# Determination of Electrolyte Transport Properties with a Multi-Reference-Electrode Cell

C. Rabette, I. Tekaya, M. Farkhondeh, B. Fleutot, Charles Delacourt

Journal of The Electrochemical Society





# Determination of Electrolyte Transport Properties with a Multi-Reference-Electrode Cell

*Journal of The Electrochemical Society*, 2021 **168** 060509

# Determination of Electrolyte Transport Properties with a Multi-Reference-Electrode Cell

**C. Rabette,[1] I. Tekaya,[2] M. Farkhondeh,[3] B. Fleutot,[1,*] and C. Delacourt[1,z]**

[1]*Laboratoire de Réactivité et Chimie des Solides, UMR CNRS 7314, Université de Picardie Jules Verne, 80039 Amiens, France*
[2]*Laboratoire de Physique de la Matière Condensée, UR EA 2081, Université de Picardie Jules Verne, 80039 Amiens, France*
[3]*Renault Technocentre, 78084 Guyancourt, France*

Fast charging is one of the main challenges of electric vehicles, partly due to electrolyte transport limitations across porous electrodes in Li-ion cells. The determination of electrolyte transport properties is crucial for modeling fast charging and adjust cell design accordingly. In this work, diffusion coefficient and cation transference number for a 1 M $LiPF_6$ in ethylene carbonate/diethyl carbonate mixture (1:1 in weight) are determined using a multireference electrode electrochemical cell (four herein). It is an extension of the work by Farkhondeh et al. [J. Phys. Chem. C 2017, 121, 8, 4112–4129] that was based on two reference electrodes. Long galvanostatic pulses allow for building up concentration gradients across the cell (restricted diffusion), which are subsequently let to relax under open circuit. The multiple voltages (three herein) measured between the four reference electrodes are simultaneously analyzed with four different procedures that involve a combination of analytic methods and nonlinear regression of the data with a numerical model. The parameter mean values and 95%-confidence intervals are evaluated using Student *t*-distribution and the bootstrap method. Values reported by combining all methods together are: $D = 2.62 \times 10^{-10}$ [± 2.29 %] $m^2\ s^{-1}$, $t_+^0 = 0.204$ [±12.25 %] at 25 °C.

 [DOI: 10.1149/1945-7111/ac03f1]

Manuscript submitted March 8, 2021; revised manuscript received April 21, 2021. Published June 8, 2021.

Supplementary material for this article is available online

## List of Symbols

| | |
|---|---|
| $c$ | salt concentration, mol $m^{-3}$ |
| $D$ | measured diffusion coefficient of electrolyte, $m^2\ s^{-1}$ |
| $(\bar{D})_B$ | average molar chemical diffusion coefficient (bootstrap estimated), $m^2\ s^{-1}$ |
| $D_{eff}$ | effective measured diffusion coefficient of electrolyte, $m^2\ s^{-1}$ |
| $\mathfrak{D}_{ij}$ | binary diffusion coefficients for interaction of species $i$ and $j$, $m^2\ s^{-1}$ |
| $F$ | Faraday's constant, 96485 C $mol^{-1}$ |
| $F_{All\Delta\Phi}$ | cost Function used for nonlinear regression |
| $\mathbf{i}$ | current density, A $m^{-2}$ |
| $i_{app}$ | current density applied to the electrodes, A $m^{-2}$ |
| $L$ | total cell thickness (excluding WE and CE), m |
| $N_i$ | total number of data points of the cost function |
| $N_M$ | McMullin Number |
| $(\bar{N}_M)_B$ | average McMullin Number (bootstrap estimated) |
| $p$ | p-value for Shapiro-Wilk's normality test |
| $q_i$ | quartiles of the data sample |
| $R$ | ideal gas constant, 8.314 J $K^{-1}$ $mol^{-1}$ |
| $R_{Ohm}$ | area-specific high frequency effective resistance of the electrolyte, Ω $m^2$ |
| $S$ | electrolyte cross section area, $m^2$ |
| $T$ | absolute temperature, K |
| $t_-^0$ | anion transference number relative to the solvent |
| $t_+^0$ | cation transference number relative to the solvent |
| $(t_+^0)_B$ | average cation transference number relative to the solvent (bootstrap estimated) |
| $t_i$ | time corresponding to timestep $i$ of simulated voltage $\Delta\Phi_s$, s |
| $V$ | potential, V |
| $V_{GF}$ | volume occupied by the glassfiber separator in the electrolyte domain, $m^3$ |
| Greek | |
| $\alpha$ | molar thermodynamic factor |
| $\epsilon$ | volume fraction of electrolyte in the separator (separator porosity) |
| $\theta_{lo}$ | lower boundary of estimated parameter $\theta$, with $\theta$ being either $D$, $t_+^0$ or $N_M$ |
| $\theta_{up}$ | upper boundary of estimated parameter $\theta$, with $\theta$ being either $D$, $t_+^0$ or $N_M$ |
| $\kappa$ | electrolyte bulk conductivity S $m^{-1}$ |
| $\kappa_{eff}$ | electrolyte effective conductivity, S $m^{-1}$ |
| $\Phi$ | electric potential, V |

In 2020, Lithium-ion batteries (LiBs) accounted for almost 200 GWh of a global battery market estimated at 500 GWh,[1] ranking as the second most predominant technology, behind the lead-acid battery (approximately 60%). For the last 30 years, its impressive market penetration has been supported by public institutions, private consumer electronics, and mobility-related ventures. This democratization trend will surely hold for several years due to the many advantages of the LiBs compared with its leading counterpart, and to the ever-increasing need for energy-storage devices. Lithium-ion technology attracts attention towards mobile applications such as electric vehicles (EVs), which require highly performant batteries to break into the mainstream market. These batteries need to meet both high-energy and high-power criteria. Intensive research and activities on new battery materials, electrolyte solutions and additives have led to an unprecedented improvement in the capacity, cycle life and cost of batteries. Today's LiBs satisfy to some extent the autonomy that is required for EVs to become a serious competitor over the conventional internal-combustion-engine (ICE) vehicles. The median drive range of EVs have increased from ca. 113 km in 2011 to 418 km in 2020.[2] However, their democratization is strongly hindered by their limited capability for fast charging compared with the time required to refuel an ICE vehicle.[3] This feature somewhat limits the use of EVs mostly to urban and suburban drivers, at least until improvements are made on both the battery pack and the charging infrastructure (e.g., DC fast-charging corridors).

In addition to the module and pack architecture, battery-cell design (e.g., electrode thickness and porosity, electrolyte type, etc.) is pivotal in determining EV chargeability. Among all, cell power is partly determined by electrolyte transport limitations that increase as

*Electrochemical Society Member.
[z]E-mail: charles.delacourt@u-picardie.fr

the thickness and density of the positive and negative electrodes increase.[4] Knowledge of the electrochemical properties of battery electrolytes is therefore required to accurately simulate the battery behavior for cell-design, control and performance-prediction purposes. From an experimental viewpoint, it may also help battery makers in the design of electrolytes, allowing to finely tune their transport properties according to the targeted application.

Complete electrochemical characterization of an electrolyte is achieved by identifying all the parameters that determine the rate of species transport in the electrolyte. According to Onsager-Stefan-Maxwell (OSM) theory, transport parameters are referred to as binary diffusivities. For a concentrated binary electrolyte (a binary salt dissolved in one solvent), there exist three diffusivities, $\mathfrak{D}_{0+}$, $\mathfrak{D}_{0-}$ and $\mathfrak{D}_{+-}$,[5] which represent binary interactions between species in the solution (subscripts 0, +, and - stand for the solvent, cation and anion, respectively). They can be combined into three measurable macroscopic parameters, namely, the ionic conductivity $\kappa$, the salt diffusion coefficient $D$ and the cation transference number $t_+^0$ with respect to the solvent velocity. The thermodynamic factor comes as an additional parameter that is required to evaluate the electrolyte non-ideality by relating the salt activity to its volumetric concentration.

These transport and thermodynamic parameters are either determined experimentally or predicted from molecular models. They are specific to each electrolyte composition and are temperature dependent. A few tens of papers[6–25] addressing characterization of LiB electrolytes have been published in the literature over the last three decades, all of which rely on tedious experiments and data-analysis procedures. Some of these research works report concentration- and temperature-dependent characterization of commonly used electrolyte formulations. Parameter estimates, however, are scarce and scattered, particularly for the transference number. In 1932, McInnes and Longsworth quoted, more specifically about the availability of transference-number data, that "the methods available for determining transference numbers have been difficult to carry out and have yielded results of low precision, even in the hands of careful workers."[26] Today, electrochemists still face the same challenge.

Several techniques have been developed and used for the determination of electrolyte transport properties. Each technique has its own degree of sensitivity and, depending on the experimental setup used, property determination may not give reproducible results. Among the available characterization methods, one can cite recurrent methods for the different transport parameters. Nuclear Magnetic Resonance (NMR) is frequently used to measure self-diffusion coefficients.[6,12,16,18,27] Darken's empirical relation can be used to estimate the binary diffusion coefficients from the measured self-diffusivity values.[16] This method uses non-trivial *a priori* assumptions and requires complex NMR facilities. In the following, focus will rather be on chemical and electrochemical methods. The thermodynamic factor $\alpha$ can be determined by several methods such as calorimetry[9] and concentration-cell experiments.[19,24,28] The ionic conductivity $\kappa$ of the solution can reliably be determined by impedance spectroscopy experiments, from the measurement of high-frequency resistance of the electrolyte.[19,25,28] The salt diffusion coefficient $D$ may be determined using restricted-diffusion experiments where the relaxation of concentration/potential gradients in the electrolyte is monitored. The relaxation process takes place following cell polarization or after two fractions of electrolyte with different concentrations are put in contact, until the two phases reach uniform concentration. Measurements can be performed in various experimental setups, including long-time voltage relaxation[11,21,25] in symmetric Li/Li electrochemical cells, refractive index change,[29] UV–vis characterization,[10] and local-conductivity change over time with Harned and French's method.[14] Finally, the transference number can be measured by techniques such as: Hittorf-cell experiments,[17] semi-infinite diffusion method by Ma et al.,[25] and the steady-state-current method by Bruce and Vincent.[15,27] Bruce and Vincent's method is valid for infinitely dilute solutions only. It has been adapted to concentrated binary electrolytes by Doyle and Newman,[30] and more recently generalized to binary electrolytes using salts comprising multivalent ions.[22] Other publications also refer to the determination of $D$ and $t_+^0$ by using "inverse-modeling" approaches. These techniques consist in analyzing experimental responses of symmetric cells to galvanostatic input currents (e.g., cell voltage[8,28] or salt-concentration profile determined using in-operando Magnetic Resonance Imaging (MRI)[13,18]) by means of a mathematical model. The transport properties (i.e., unknown model parameters) result from the best fit of the model to the experimental data achieved using an optimization algorithm. However, electrochemical methods involving galvanostatic experiments usually rely on two-electrode cells using metallic lithium as working/counter electrodes where current is applied and potential difference is recorded. During current application, the voltage response of such a cell is conditioned by hardly determinable surface overpotentials that depend on experimental setup conditions. Lithium is, in addition, well known for its high reactivity towards electrolyte and its propensity for dendrite growth.[31] These phenomena induce strong unpredictable perturbations in the cell voltage,[32,33] and prevent exploitation of the closed-circuit voltage response. Hence, experimental data from two-electrode cells used for inverse-modeling procedures are limited to open-circuit voltage (OCV).

In 2016, Farkhondeh et al. reported on a new characterization method[34,35] for binary electrolytes that combines inverse modeling with a novel electrochemical cell architecture featuring two reference electrodes in addition to the working and counter electrodes. A major difference compared with prior works is the possibility of using closed-circuit voltage (CCV) for data processing, allowing for the simultaneous determination of $D$, $\kappa$ and $t_+^0$.

The present work proposes electrolyte characterization using a multi-electrode cell comprising working/counter electrodes and more than two reference electrodes, developed on the same basis as the aforementioned four-electrode cell. In the following, the architecture of the multi-electrode cell is first presented and its working principle is detailed. A commercial battery electrolyte, here a 1M solution of $LiPF_6$ in EC/DEC (1:1 weight proportions), is eventually characterized at 25 °C. Because the electrolyte in the multi-electrode cell is supported by a separator, the McMullin number of the separator $N_M$ (quantifying the impact of the separator on the measured transport properties) is reported, together with $D$ and $t_+^0$. $N_M$ is calculated in the following from two independent measurements of $\kappa$ and $\kappa_{eff}$. Different data-processing approaches are investigated and the reliability of the multi-electrode method is assessed by evaluating the confidence intervals of the estimated transport properties.

## Experimental Setup

***Reminder about the four-electrode setup.***—The idea of a four-electrode device under galvanostatic conditions was proposed in 1993 in the context of solid electrolytes for lithium batteries.[36] Some other works report on pouch-type "Lithylene" lithium-ion batteries equipped with micro reference electrodes for in-operando monitoring of concentration gradients.[37]

More recently, Farkhondeh et al. introduced a four-electrode cell design for the characterization of liquid binary electrolytes.[34,35] Although care is needed for the implementation of this device in the case of liquid electrolytes, the technique proved efficient for isobaric and isothermal evaluation of transport parameters. A schematic of this cell is shown in Fig. 1a. Figure 1b illustrates the main improvement of this method over the state of the art, namely the ability to measure a voltage response between the reference electrodes (blue line on Fig. 1b) even during closed-circuit periods, hence, avoiding kinetic contributions of the working and counter electrodes (dashed grey line on Fig. 1b).

The cell architecture proposed in this work is developed on the same basis as the four-electrode cell,[34,35] using four reference

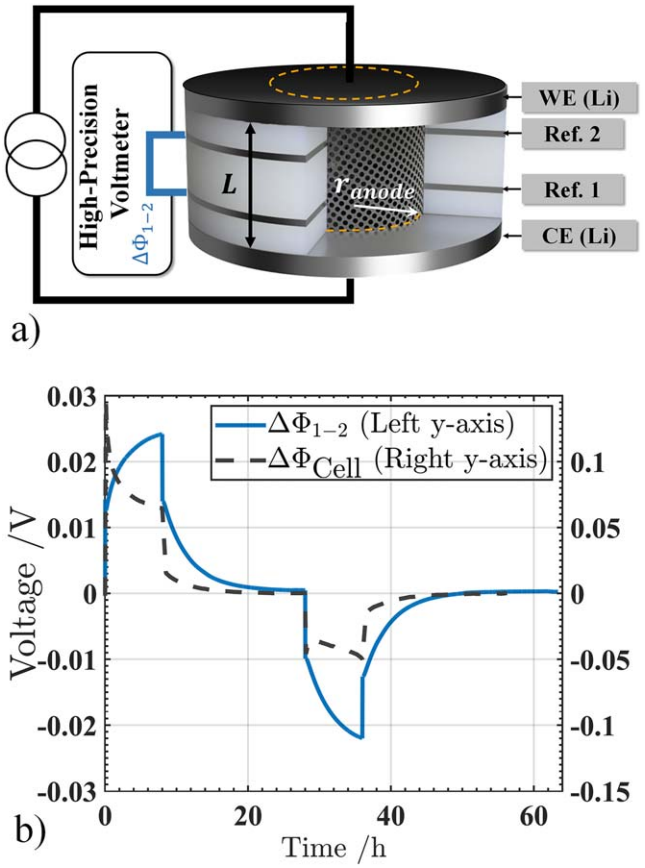


**Figure 1.** (a) Schematic representation of a cylindrical 4-electrode cell, designed for electrolyte-property measurement, as reported by Farkhondeh et al.[34,35] (b) Experimental voltage signals measured between the working and counter electrodes (dashed grey line) and between the reference electrodes (solid blue line). The signal measured between the reference electrodes is used for electrolyte characterization.

electrodes instead of just two, allowing for the measurement of three voltage signals across the cell length. A schematic diagram of the multi-electrode cell is shown in Fig. 2b. When a current pulse is applied to the cell, potential profiles establish progressively with time in the electrolyte volume, as shown in Fig. 2a.

***The six-electrode cell.—***The cell consists of two lithium-metal (Li) working and counter electrodes, separated by a stacked polymer-spacer and reference-electrode array of a known thickness. This stack is composed of high-density polyethylene (HDPE) round flat washers (Bülte company, Germany) of 12.8 mm inner diameter, 25.4 mm outer diameter and 1.05 mm thickness, and Li round, flat-washer-shaped reference electrodes. The reference electrodes are prepared by punching a circular piece out of a Li ribbon (GoodFellow: 99.99% purity, 35 mm wide and 0.2 mm thick) at the center of which a circular hole of 12.8 mm is punched. 14 μm thick, 3 mm wide and 20 mm long copper foil strips are then crimped to the Li rings used for voltage sensing. The spacer/reference-electrode array comprises five HDPE spacers and four Li references (Fig. 2b), forming a hollow cylinder with an inner diameter of 12.8 mm and a height of 6.05 mm. Several layers of a glassfiber separator (Whatman GF/D) are piled up inside this empty volume, so as to mitigate effects of convection in the electrolyte, after being carefully dried up under vacuum. In this work, a 1M $LiPF_6$ in EC/DEC (1:1 in weight) commercial electrolyte (Merck, Germany) is used. Density of the separator is measured by gas pycnometry (Micrometrics AccuPyc 1330, USA) to be 2.503 g $cm^{-3}$ at 25 °C. Knowing the weight of the separator layers, the porosity of the separator stack that is eventually filled up with the electrolyte, is estimated to be $\epsilon = 1 - \frac{V_{GF}}{SL} = 0.955$. $S$ stands for the cross-section area of the inner cylinder formed by the HDPE/Li washers stack, $L$ is the total thickness of the stack and $V_{GF}$ is the volume occupied by the piled-up glassfiber separators. Accordingly, the volume of electrolyte needed to fill the separator is estimated to be: $V_e = \epsilon SL = 748$ μL. Reference electrodes are numbered from "Ref. 1" to "Ref. 4" (Fig. 2b) to ease their identification, with "Ref. 1" being located closest to the bottom electrode (counter electrode). The cell is made airtight using multiple O-ring gaskets made of fluorocarbon (i.e., FKM or Viton™).

***Electrochemical experiments.—***Assembly of the airtight cell and electrochemical experiments are performed under dry air (−58 °C maximum dew point) in a Memmert IPP55 temperature chamber, with a setpoint temperature at 25 °C.

Electrochemical characterization of the electrolyte is performed using galvanostatic cycling experiments. A sequence of alternatively positive and negative eight-hour current pulses is applied to the cell. The applied current density is set to $|i_{app}| = 1.87$ A $m^{-2}$ during pulses 1 to 4 and pulses 9 and 10. A different current density of $|i_{app}| = 4.97$ A $m^{-2}$ is applied during pulses 5 to 8. Operating conditions are such that concentration gradients form across the cell without exceeding concentration differences of ca. ± 0.1 mol $L^{-1}$ and ± 0.160 mol $L^{-1}$ with respect to the initial electrolyte concentration between the outermost reference electrodes (according to data analysis with a mathematical model) for the 1.87 and 4.97 A $m^{-2}$ pulses, respectively. Between each current pulse, a 35-hour open-circuit rest period is set so that concentration gradients fully relax.

Cell voltage is measured during the closed-circuit and open-circuit periods using a Biologic VSP potentiostat. For these experiments, the potentiostat is connected to the cell in the three-electrode fashion, using Ref. 1 as the reference. A Keysight 34972A digital precision multimeter equipped with a 34901A multiplexing board is used for measuring voltages between Ref. 1 and Ref. 2 ($\Delta\Phi_{1-2}$), Ref. 1 and Ref. 3 ($\Delta\Phi_{1-3}$), and between Refs. 1 and 4 ($\Delta\Phi_{1-4}$).

Effective conductivity of the electrolyte $\kappa_{eff}$ is initially measured by potentiostatic electrochemical impedance spectroscopy (EIS) at frequencies ranging from 200 kHz down to 10 mHz. Area-specific high-frequency resistance (i.e. $R_{Ohm}$, real-part of the complex impedance at 200 kHz multiplied by the area of the working electrodes) is attributed to the effective ohmic resistance of the electrolyte.

The multi-electrode cell only allows for measuring effective transport properties ($D_{eff}$ and $\kappa_{eff}$) because the electrolyte is supported by the glassfiber separator. The geometrical properties of the separator are quantified through its McMullin number defined as $N_M = \tau/\epsilon = \kappa/\kappa_{eff} = D/D_{eff}$ where $\tau$ and $\epsilon$ are the separator tortuosity and porosity, respectively. Evaluation of $N_M$ thus requires an independent measurement of either the values of $D$ or $\kappa$. In this work, the bulk electrolyte conductivity $\kappa$ is measured using a lab-designed conductivity cell coupled to a frequency analyzer (sensing up to 30 MHz). Its value is measured to be $\kappa = 0.795$ S $m^{-1}$ at $T =$ 25 °C, in good agreement with a prior work.[28]

## Theory

The additional reference electrodes of the multi-electrode cell allow for probing delimited portions of thickness of the separator that indirectly provide information about composition variations across the electrolyte with the aid of a model-based experimental-data analysis. Ion transport in such an electrochemical cell is described using a mathematical model derived from concentrated-solution theory, as described below. The model relies on a set of equations involving three transport parameters (in the case of a binary electrolyte) and the thermodynamic coefficient.

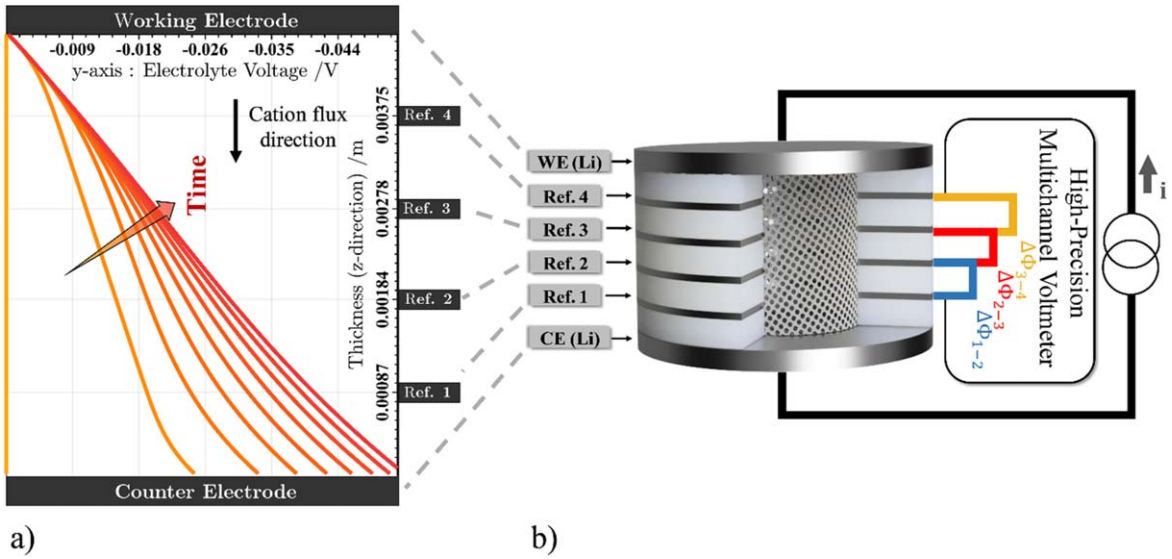


**Figure 2.** (a) Time-dependent representation of the electrolyte potential evolution across the cell length under galvanostatic condition. The electrolyte potential is set to 0 V at the working-electrode boundary. (b) Schematic representation of a six-electrode cell. The reference electrodes are connected to a high-precision multiplexing voltmeter, which allows for the simultaneous measurement of all voltage signals over time.

***One-dimensional mass transport model for concentrated binary electrolytes.***—The model is based on Onsager-Stefan-Maxwell (OSM) transport formalism for multicomponent diffusion, applied to a binary electrolyte. Adequate reworking of OSM flux-explicit equations, neglecting convection phenomena in the electrolyte volume, yields the McInnes transport equation:[5]

$$\mathbf{i} = \kappa_{\text{eff}}\left[-\nabla\Phi + \frac{2RT}{F}\alpha(1 - t_+^0)\nabla \ \ln \ c\right] \qquad [1]$$

with $c$ being the salt concentration in the electrolyte, $\Phi$ the electrolyte potential and $\mathbf{i}$ the ionic current density. $\kappa_{\text{eff}}$ is the effective ionic conductivity of the electrolyte (i.e. corrected for McMullin number $N_{\text{M}} = \tau/\epsilon = \kappa/\kappa_{\text{eff}}$), $t_+^0$ the transference number of the cation relative to the solvent, $R$ the ideal gas constant, $T$ temperature and $F$ Faraday's constant. $\alpha = \left(1 + \frac{d \ln f_\pm}{d \ln c}\right)$ is the thermodynamic factor, with $f_\pm$ being the mean molar activity-coefficient of the salt at a given composition. Mass conservation reads:

$$\epsilon\frac{\partial c}{\partial t} + \nabla\cdot\left(-D_{\text{eff}} \ \nabla \ c - \frac{(1 - t_+^0)\mathbf{i}}{F}\right) = 0 \qquad [2]$$

where $D_{\text{eff}} = \frac{\epsilon}{\tau}\mathscr{D}\frac{c_{\text{T}}}{c_0}\alpha$ is the molar effective diffusion coefficient, $\mathscr{D}$ is the thermodynamic diffusion coefficient, related to the binary diffusivities $\mathfrak{D}_{ij}$. $c_{\text{T}}$ and $c_0$ are the total and solvent concentrations, respectively.

Charge conservation in the electrolyte is described by:

$$\nabla\cdot\mathbf{i} = 0 \qquad [3]$$

Ion transport in the electrolyte is simulated in this work using a one-dimensional model constituted by Eqs. 1–3. This model requires four boundary conditions (BCs) for proper closure. The current density $\mathbf{i}$ is set equal to the input current $i_{\text{app}}$ at the counter electrode boundary while the electrolyte potential $\Phi$ is set to zero at the working electrode boundary. Two other BCs are addressed by setting the anion flux to zero at both electrodes (as $PF_6^-$ ions are not involved in redox reactions with Li). Salt concentration is initially set to $c = 1000$ mol m$^{-3}$ across the electrolyte domain. The net current passing through the reference electrodes is equal to zero, and so, these electrodes are not explicitly modeled in this 1D model. Because the electric potential of the electrolyte is defined based on the Li metal reference electrode, the electric potential difference measured between two reference electrodes corresponds to that of the electrolyte.

***Influence of transport parameters on the measured voltage.***—Figure 3 shows simulated voltage signals typically measured between reference electrodes of a multi-electrode cell. In this figure, the domains of influence of each of the transport properties ($D_{\text{eff}}$, $t_+^0$ and $\kappa_{\text{eff}}$) are shown using grey arrows and corresponding labels.

***Conductivity.***—Application of a current between the working electrodes induces a voltage drop at the onset of the pulse (Fig. 3). At the early stage of the pulse, Eq. 1 reduces to $\mathbf{i} = -\kappa_{\text{eff}} \ \nabla\Phi$, which corresponds to Ohm's law, as no concentration gradient has developed in the cell yet. The six-electrode cell may be used to determine the electrolyte effective conductivity through high-frequency EIS experiments as well as galvanostatic experiments, using this equation. No difference is made in the following on whether the area-specific effective resistance of the probed portion of electrolyte $R_{\text{Ohm}}$ is measured in the time- or frequency-domain as it stands for the same quantity. EIS measurements give direct access to the effective area-specific ionic resistance of the electrolyte at high frequency $R_{\text{Ohm}}$ (Fig. 4). In the time domain, the area-specific effective resistance is computed according to $R_{\text{Ohm}} = \Delta V/|i_{\text{app}}|$, where $\Delta V$ is the voltage drop measured between two reference electrodes at the pulse-onset, $|i_{\text{app}}|$ is the magnitude of the current density applied to the cell.

The voltage drop measured in the cell is proportional to the probed length $l$, hence, by virtue of the equation for the resistance of a cylindrical conductor:

$$R_{\text{Ohm}} = \frac{l}{\kappa_{\text{eff}}} \qquad [4]$$

By plotting the values of the electrolyte area-specific effective resistance $R_{\text{Ohm}}$ as a function of the probed distance in the cell, an estimation of the electrolyte resistivity is obtained (Fig. 4a). All

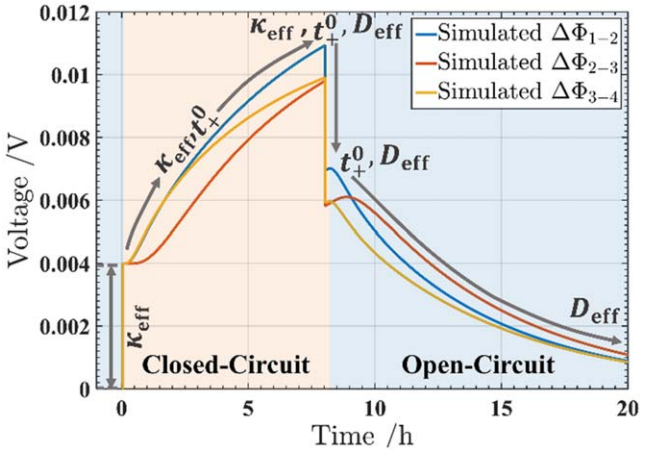


**Figure 3.** Simulated typical voltage signals between three reference-electrode couples: $\Delta\Phi_{1-2}$, $\Delta\Phi_{2-3}$ and $\Delta\Phi_{3-4}$. This simulation is based on a cell consisting of Li electrodes under galvanostatic conditions (CCV) followed by a rest period (OCV). Electrolyte properties are taken from Lundgren et al.[28] Grey arrows emphasize the domains of influence for the three transport parameters.

available pairs of electrodes are probed, each corresponding to a given distance in the cell (Fig. 4b). The quality of the linear dependence of $R_{Ohm}$ on $l$ provides a figure of merit for the cell assembly.

***Diffusion coefficient.—***During relaxation, the concentration gradients that formed during current pulses relax back to eventually yield a uniform concentration across the cell. As no net current flows during the open-circuit step, the rate of decrease of the voltage logarithm is, after long-enough time, exclusively driven by diffusion across the electrolyte.[29] $D_{eff}$ is thus determined by monitoring the OCV between pairs of reference electrodes. For this restricted-diffusion system, the value of $D_{eff}$ is determined using Eq. 5:[25,29]

$$slope_{D_{eff}} = \frac{d(-\ln|\Delta\Phi|)}{dt} = \frac{\pi^2 D_{eff}}{L^2} \qquad [5]$$

where $\Delta\Phi$ is the monitored voltage signal during relaxation, $D_{eff}$ is the effective salt diffusion coefficient, and $L$ is the total length of the cell over which concentration gradients formed. This simple method is used in this work for the determination of the diffusion coefficient using the six-electrode cell. The diffusion coefficient may as well be determined from an inverse-modeling method which is described in the following. Comparison will then be made between values derived from the two methods.

***Transference number.—***The CCV response of the cell depends on $D$, $t_+^0$, and $\kappa$ altogether. State-of-the-art methods are usually not appropriate to analyze CCV[8,24,28] because the working and counter electrodes of such cells are subjected to faradaic reactions, inducing surface overpotentials that highly depend on the electrodes and the operating conditions. Moreover, interfaces between the working electrodes and the electrolyte are subject to complex phenomena such as dendrite formation, passivation-layer growth and dead Li trapped in Li moss that substantially distort the measured cell-voltage response in conventional two-electrode cells.

In this work, $t_+^0$ is measured using an inverse-modeling technique, which consists in minimizing the sum of squared errors between simulation results and experimental data obtained over both closed-circuit and open-circuit steps. The regressed parameters are those corresponding to the best fit between the simulation and experiment. Nonlinear regression is performed using the "trust-region" algorithm implemented in *lsqnonlin* built-in function from *Matlab* software. Simulations are performed using a 1D simulation software developed by Delacourt,[38] based on Newman's battery model.[39]

In the following, the nonlinear regression is performed using a cost-function $F_{All\Delta\Phi}$, defined as:

$$F_{All\Delta\Phi} = \frac{1}{N_i}\sum_{i=1}^{N_i}(\Delta\Phi_e - \Delta\Phi_s(t_i|\{t_+^0, D, N_M\})^2 \qquad [6]$$

Where $N_i$ is the total number of data points and $t_i$ is the time value corresponding to timestep $i$ of the numerical solution. The nomenclature of this function emphasizes that all voltage signals $\Delta\Phi_{1-2}$, $\Delta\Phi_{2-3}$ and $\Delta\Phi_{3-4}$ are involved in the calculation of the squared residuals between the simulated ($\Delta\Phi_s$) and experimental ($\Delta\Phi_e$) signals.

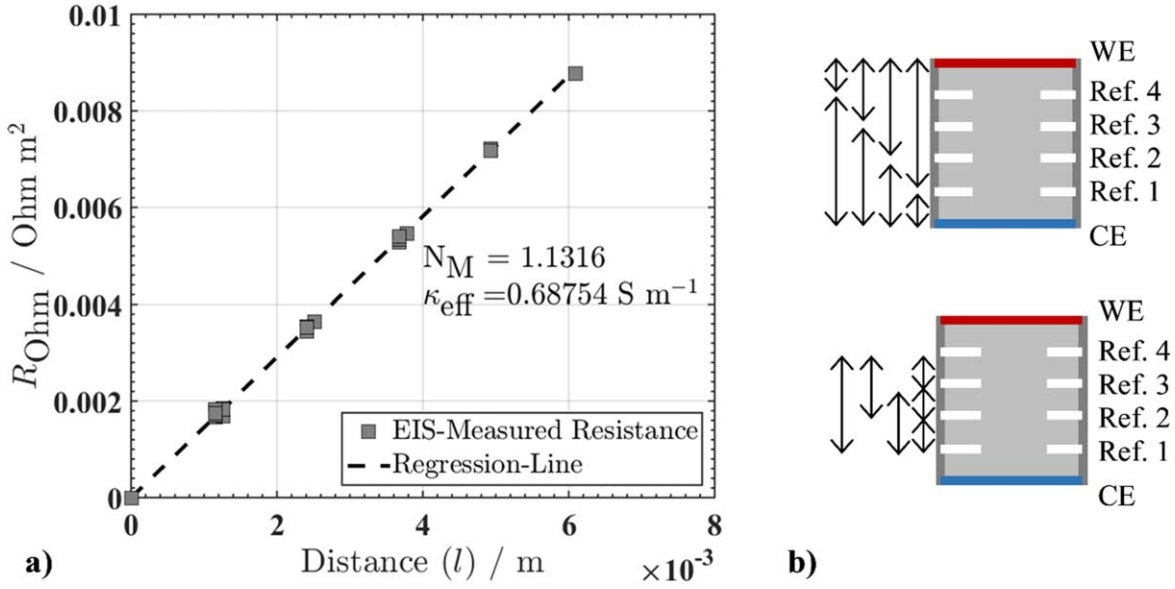


**Figure 4.** Determination of $\kappa_{eff}$ (so as to derive $N_M$) using the six-electrode cell, with a glassfiber separator filled with 1M $LiPF_6$ in EC/DEC (1:1 weight). (a) Area-specific effective resistance $R_{Ohm}$, measured using EIS at high frequency (200 kHz), vs probed electrolyte thickness $l$. b) Pairs of electrodes used for the EIS measurements.

## Results and Discussion

An advantage of using multiple voltage traces is the improved robustness of the estimated transport properties. The reliability of the dataset is also assessed by comparing the experimental signals with one another and evaluating their agreement with theoretical expectations. Moderate values of current densities are applied, which simplifies subsequent data processing by assuming that the transport parameters are constant in the limited range of concentrations that develop across the cell.

Figure 5 represents experimental voltage responses of the six-electrode cell to the applied current pulses, for pulses 2 (Figs. 5a and 5c) and 3 (Figs. 5b and 5d). Figures 5a and 5b show the signals measured between couples of reference electrodes 1–2, 1–3 and 1–4. Another representation is used in Figs. 5c and 5d wherein the signals are measured between reference couples 1–2, 2–3 and 3–4. Simulated signals are also plotted in Figs. 5c and 5d with dashed lines for visual comparison between theoretically-expected and real-life shapes of the reference-measured signals. The cell voltages, measured between the working and the counter electrodes, are also displayed in each panel (solid grey lines). As emphasized on the plot of adjacent-electrode responses in Figs. 5c and 5d, the voltage signals between reference electrodes show substantial deviations from simulated signals. These flaws are mainly attributed to the nonuniform reaction dynamics on the surface of the Li working electrodes. Even though reference electrodes are supposedly insensitive to working-electrode kinetics, it goes a different way in practice.[40,41] Nonuniform faradaic processes occurring at the working electrodes influence the current lines across the electrolyte.[7,32,42–44] These nonideal current lines hence distort the voltage measured between the reference electrodes. Figure 6 shows the cell potential signals, for pulse 2, measured in a 3-electrode fashion, using "Ref. 1" as a reference electrode. Traces of $\Delta\Phi_{1-\mathrm{WE}}$ and $\Delta\Phi_{1-\mathrm{CE}}$, represented in Fig. 6a display unexpected features, which may be attributed either to the working or the counter electrode, respectively. These voltage surges are ascribed in the literature to different phenomena,[32,42–44] as labeled in Fig. 6a. Both contributions show up on the $\Delta\Phi_{\mathrm{Cell}}$ signals in Figs. 5 and 6b. For instance, the voltage surges observed on $\Delta\Phi_{\mathrm{Cell}}$ in Fig. 5 after ca. seven hours of applied current, are ascribed to the depletion of the previously plated active Li and the subsequent formation of pits on the surface of the metallic bulk Li that has not cycled yet,[32,42–44] as suggested by three-electrode cell-voltage measurements (Fig. 6). Figure 5 indeed shows that this phenomenon, which is visible on all three $\Delta\Phi_{1-2\ldots4}$ signals in panels a and b, is more clearly seen on $\Delta\Phi_{1-2}$ in panel c and on $\Delta\Phi_{3-4}$ in paneld. This observation is well in line with previously-stated hypotheses, keeping in mind that $\Delta\Phi_{1-2}$ and $\Delta\Phi_{3-4}$ probe the electrolyte portions at the vicinity of respectively the counter and the working electrodes which are being oxidized during pulses 2 and 3.

It is also worth noting this is only true when already-cycled Li exist at the surface of the electrodes (pulse number >1). No such mid-pulse surge is observed on the cell-voltage traces of pulse 1. This is likely due to the pristine, dendrite-free, Li surfaces of the working electrodes, before applying any current. Instead, substantial voltage surges are observed, at the onset of the working- and counter-electrode signals, from three-electrode measurements (not presented here). It is hypothesized that both Li stripping at the working and Li plating at the counter electrodes contribute to these voltage anomalies. The spikes at the onset of cell-voltage signals remain over the subsequent pulses. Figure 6 shows that, unlike pulse 1, these onset surges are attributed only to Li plating at the electrode that reduces. This is also manifested in $\Delta\Phi_{3-4}$ data in Fig. 5c (pulse 2) and in $\Delta\Phi_{1-2}$ data in Fig. 5d (pulse 3).

These phenomena appear consistently when using metal Li as working electrodes. Although following obvious trends, the effects of these voltage surges on signals measured between the reference electrodes are not accounted for in a quantitative fashion by the current model. A decorrelation between the flawed signals and an average "flawless" trend is thus impossible.

Hence, as highlighted in the following, computed values of the transport properties, using these data, shall be affected by the

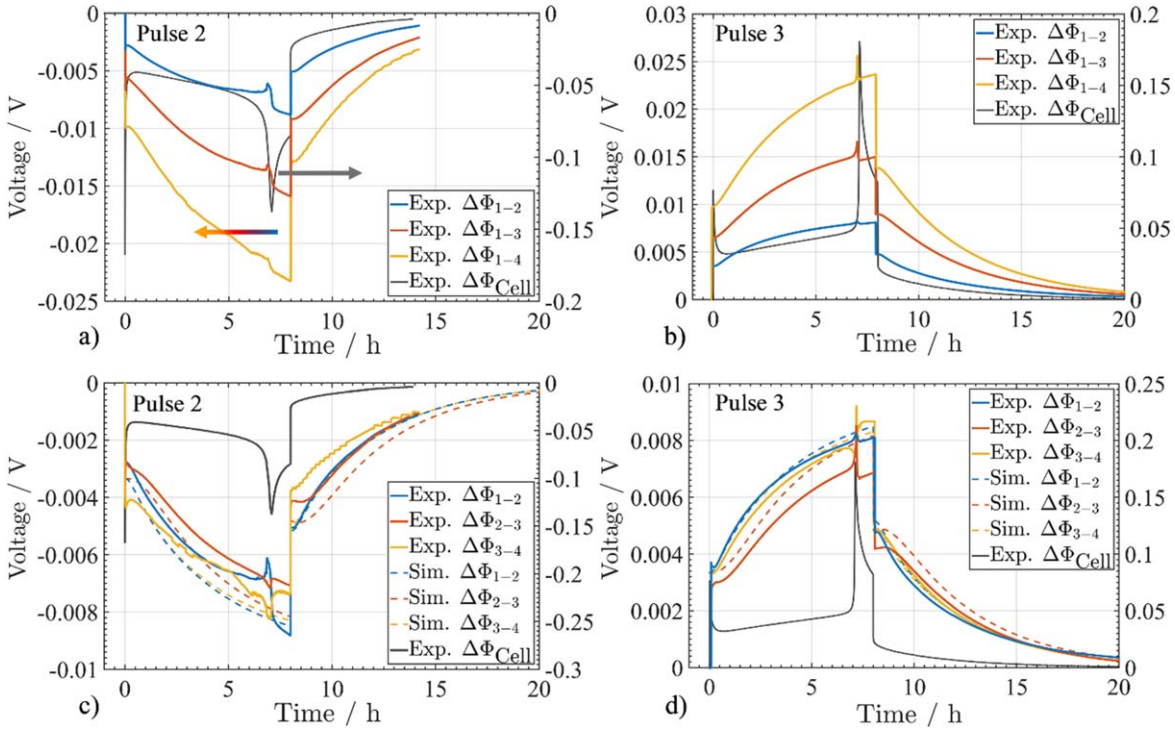


**Figure 5.** Voltage traces measured between (a), (b) reference pairs 1–2, 1–3 and 1–4, and (c), (d) 1–2, 2–3 and 3–4. These voltage traces correspond to pulse 2 (a), (c) and pulse 3 (b), (d). Cell voltage appears as a solid grey line. The Li-symmetric cell is subjected to a current pulse of magnitude $|i_{\mathrm{app}}| = 1.87$ A $\mathrm{m}^{-2}$ for 8 h, followed by a relaxation time. Dotted lines in (c), (d) stand for simulated signals.

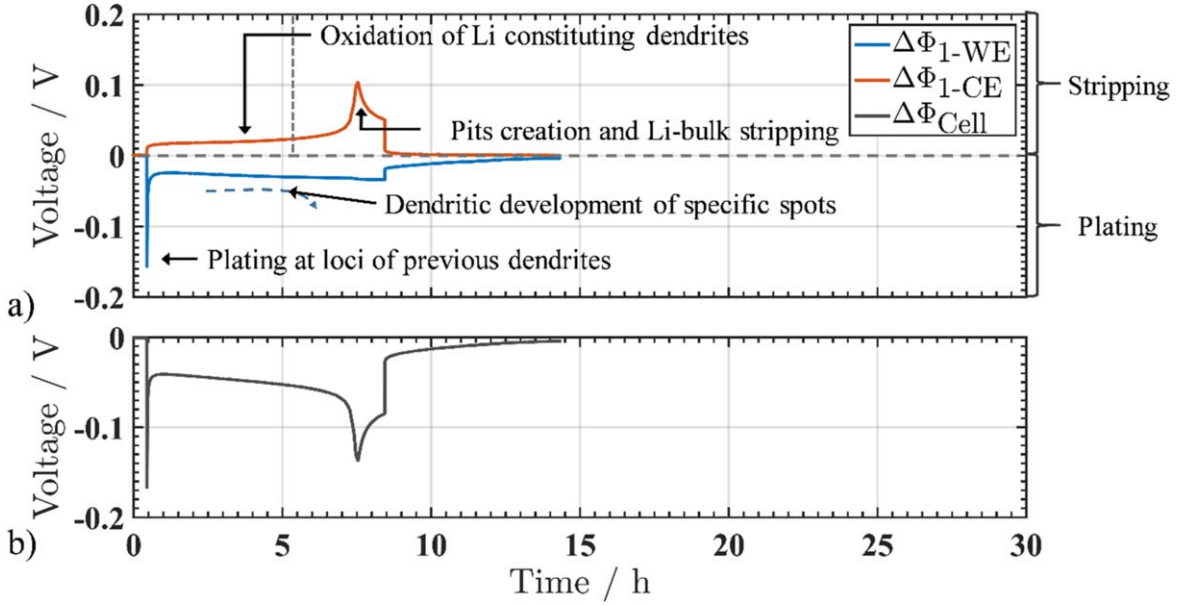


**Figure 6.** Three-electrode data corresponding to the WE and CE voltages measured vs Ref. 1 during pulse 2. (a) $\Delta\Phi_{1-WE}$ and $\Delta\Phi_{1-CE}$ traces vs time and emphasis of the different phenomena occurring during cycling (responsible for remarkable features on the voltage signals). (b) $\Delta\Phi_{Cell}$ corresponding to the subtraction of $\Delta\Phi_{1-CE}$ to $\Delta\Phi_{1-WE}$.

aforementioned distortions in voltage signals measured between the reference electrodes. Furthermore, as the onset-voltage surge of pulse 1 is substantially larger than on other pulses, model-parameter estimation leads to outlier values of the transport properties. The first pulse of the galvanostatic sequence is thus discarded in the following of this study.

***Effective conductivity.***—Although the data points at the onset of experimental data are likely affected by uncontrolled reaction dynamics at the working electrodes, neighboring points may be considered to be "reasonably accurate" for effective-resistance measurement. To this end, the data points are selected thirty seconds after the circuit is closed, partly avoiding the initial voltage surge. These selected points (grey square markers in the inset of Fig. 7 and in the main frame, for the third pulse) are used to derive $R_{Ohm} = f(l)$, as shown in Fig. 7, of which the slope corresponds to the inverse of effective conductivity $1/\kappa_{eff}$, according to Eq. 4.

The linear regression represented in Fig. 7 yields a value of $\kappa_{eff} = 0.720$ S m$^{-1}$ for the effective conductivity, corresponding to a McMullin number value of $N_M = 1.08$. This conductivity evaluation may be appended by the impedance spectroscopy measurements of the $R_{Ohm}$ between all pairs of reference electrodes (Fig. 4b) and similar data processing (Fig. 4a). EIS data yield a value of 1.13 for the McMullin number. As shown in the following, both of these values are in good agreement with the distribution of values of $N_M$ observed for all the pulses.

***Effective diffusion coefficient.***—As developed in the theoretical section, the multi-electrode cell allows the measurement of $D_{eff}$ using Eq. 5. The electrolyte diffusion coefficient $D$ is derived from $D_{eff}$, according to $D = N_M D_{eff}$. Prior computation of $N_M$ (from the ratio of $\kappa$ and $\kappa_{eff}$) is thus necessary to derive $D$.

Figure 8 shows how the effective diffusion coefficient is derived from the slopes of $\ln|\Delta\Phi|$ vs t (Eq. 5) at long time. Values of $D_{eff}$ are reported in Figs. 8a and 8b for the third and fourth pulses. An average value is derived from these local $D_{eff}$ coefficients, for each pulse. However, $\ln|\Delta\Phi_{1-2}|$ departs from the straight-line behavior at long time (noticeable in Fig. 8a), which was also reported early on by Farkhondeh et al.[35] The $\Delta\Phi_{1-2}$ signals are thus discarded in the following for the computation of $D_{eff}$ using Eq. 5.

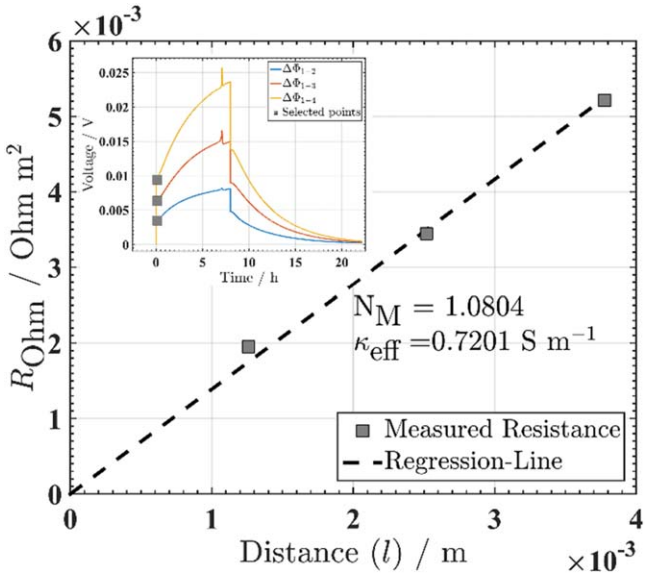


**Figure 7.** Evaluation of the effective conductivity of the electrolyte soaked in the separator, using "short-time" data of $\Delta\Phi_{1-2}$, $\Delta\Phi_{1-3}$ and $\Delta\Phi_{1-4}$ signals from pulse 3 (represented in Fig. 5b and reminded as an inset). The area-specific effective resistance $R_{Ohm}$ corresponding to the selected points is plotted vs reference-electrode spacing. The slope of this line provides direct information about the effective conductivity. The grey square markers in the figure inset indicate the data points selected for McMullin-number evaluation.

***Transference number.***—The McInnes Eq. 1 relates the current density $\mathbf{i}$ to the product $\alpha(1 - t_+^0)$, where $\alpha$ stands for the thermodynamic factor of the solution. The determination of this product is thus required, prior to determining the transference number of the binary electrolyte. Measurement of $\alpha(1 - t_+^0)$ is conducted using concentration cells (see Supporting Information, available online at stacks.iop.org/JES/168/060509/mmedia), processing data using the protocol outlined by Lundgren et al.[28] $t_+^0$ is evaluated with an inverse-modeling method,

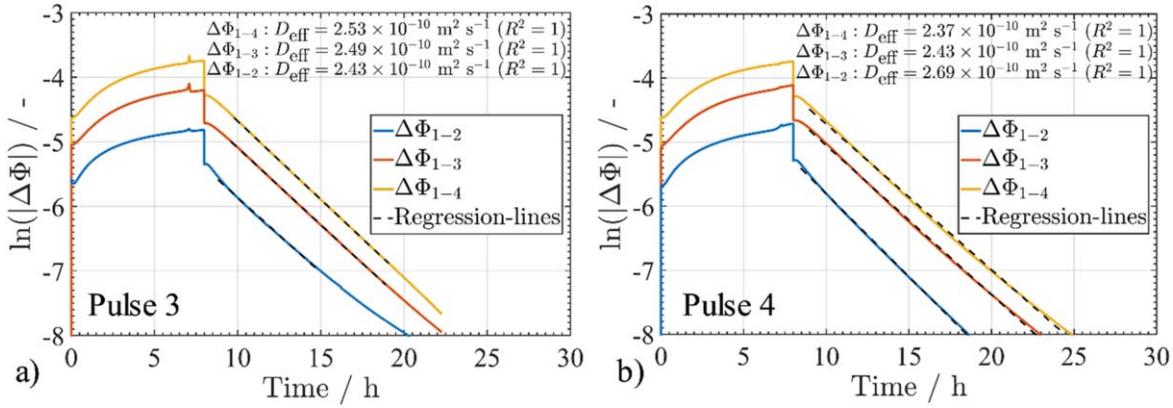


**Figure 8.** ln(|ΔΦ|)-time representation of $\Delta\Phi_{1-2}$, $\Delta\Phi_{1-3}$ and $\Delta\Phi_{1-4}$ for (a) pulse 3 and (b) pulse 4.$D_{\text{eff}}$ is derived from the slope of the three parallel straight lines, according to Eq. 5.

using previously-determined parameters ($\kappa_{\text{eff}}$ and $D_{\text{eff}}$) and the measured value of $\alpha(1 - t_+^0)$ as input for the model.

***Numerical optimization.***—Ten galvanostatic pulses are successively applied to the cell. For pulses 2 to 10, the transport parameters are estimated using four independent procedures. Optimization strategy I corresponds to the fitting of all transport parameters ($D$, $t_+^0$, $\kappa_{\text{eff}}$) using a nonlinear regression algorithm. In procedure II, $D$ is determined using Eq. 5, while $t_+^0$ and $\kappa_{\text{eff}}$ are obtained by nonlinear regression. Procedure III corresponds to the nonlinear regression of $t_+^0$ only, while $D$ and $\kappa_{\text{eff}}$ are estimated using Eqs. 5 and 4, respectively. Finally, procedure IV corresponds to the nonlinear regression of $D$ and $t_+^0$, coupled with the estimation of $\kappa_{\text{eff}}$ using Eq. 4. In each procedure, when a parameter is adjusted, its lower and upper bounds are set such that: $0 < \kappa_{\text{eff}} < 1.00$ S m$^{-1}$, $1.00 \times 10^{-11} < D < 1.00 \times 10^{-9}$ m$^2$ s$^{-1}$ and $0 < t_+^0 < 1.00$. As the main interest for determining $\kappa_{\text{eff}}$ is the computation of the associated McMullin number, $N_{\text{M}}$ is systematically reported in the following instead of $\kappa_{\text{eff}}$.

Figure 9 shows a comparison between different regression procedures used to fit the model to experimental data, for the first four pulses. The signals are plotted using a logarithmic scale on the $y$ axis for a better readability between the different lines. Each line style in the four panels of Fig. 9 is specific to a procedure number (Table I) employed for determining the simulation-input transport properties (dashed, dashed-dot, and dotted lines refer to I, II, and III, respectively). The dashed-dotted purple line on Fig. 9a is the signal simulated with the parameters regressed using procedure II, cost-function $F_{\text{All}\Delta\Phi}$ and discarding the first 30 s of $F_{\text{All}\Delta\Phi}$. The dashed-dotted grey line corresponds to similar conditions, this time ignoring the first 5 min of $F_{\text{All}\Delta\Phi}$. This cost-function trimming aims at ignoring the already mentioned parasitic phenomena occurring at the beginning of the pulses, by removing their contribution to the cost function. Pulse 1 (Fig. 9a), although not being included in the dataset for parameter-estimation, is a good example for illustrating the influence of this trimming operation because its onset potential surge is exacerbated, as already discussed early on. After a comparison between the regression output from the two cases, the 5-minute trimming of $F_{\text{All}\Delta\Phi}$ (grey lines in Fig. 9) is selected for all regression procedures.

Table I summarizes the computed transport parameters, averaged over all-nine pulses (pulses 2–10), according to each procedure. The procedures combine nonlinear least-square regression and analytic solutions of Eqs. 4 and 5. Roman numerals I to IV in the table refer to the optimization strategies mentioned hereinbefore. The relative errors on the parameters are also indicated between brackets. These errors are computed using the bootstrap method as explained in the following. While numbers in Table I display substantial variations, depending on the procedure used for the determination of transport-properties, Figs. 9b–9d show that the corresponding simulation results are almost overlapping. Figure 10 shows the variations of the quality of the fit among the 4 parameter-estimation procedures. The figure shows that the value of $F_{\text{All}\Delta\Phi}$ at the end of the regression process is, in average, quite similar for all procedures. This may be explained for the major part by the distortions of the voltage signals measured between the reference electrodes, arising from parasitic reaction at the working electrodes. In addition to their impact on the regressed signals, these irregularities induce flaws in the determination of the analytically-computed parameter values in procedures II and mainly III and IV. For example, the determination of $N_{\text{M}}$ turns out to be more sensitive to signal contamination from working electrodes than $D_{\text{eff}}$, which is determined after long-enough relaxation periods. Such flawed values of $N_{\text{M}}$ depend on the magnitude of the voltage spikes at the onset of the closed-circuit steps. An overestimated $N_{\text{M}}$ may induce an artificial increase in the estimated values of $t_+^0$. The value for $D$ may as well be impacted, both directly because $t_+^0$ is overestimated, and indirectly because $D$ is computed using $N_{\text{M}}$.

It is shown in Fig. 10 and Table I that whether $D$ is computed analytically or by nonlinear regression does not make a large difference in the quality of the fits and the error associated with the determined parameters (comparing results from procedures I and II). However, separate estimation of $N_{\text{M}}$ is detrimental to the goodness of fit (comparing results from procedures III and IV). Indeed, although the median looks relatively independent of the fitting procedure used, the distribution skewness of $F_{\text{All}\Delta\Phi}$ $(i_{\text{app}}S)^{-2}$ is considerably enhanced for procedures III and IV. These moderately to highly skewed $F_{\text{All}\Delta\Phi}$ $(i_{\text{app}}S)^{-2}$ distributions suggest that the squared residuals $F_{\text{All}\Delta\Phi}$ are not exclusively driven by random fluctuations and support the hypothesis of reference-electrode signal contamination by the working electrodes.

Results of all regressions are summarized in Fig. 11 where the fitted parameters are plotted as a function of pulse number and the fitting procedure (Figs. 11a–11c). A procedure-wise outlook of the distributions of the transport-property values is provided using boxplots (Figs. 11d–11f). Two main correlations emerge (not shown herein) from this dataset: a positive correlation between the fitted values of $t_+^0$ and $N_{\text{M}}$, and a negative correlation between $t_+^0$ and $D$. Figure 12 gathers the experimental voltage signals, measured for pulses 2 to 10. Two representations are included in the figure, with the main panels showing the signals measured between pairs of reference electrodes 1–2, 1–3 and 1–4 and the inset views in each panel showing the signals measured between pairs of reference electrodes 1–2, 2–3 and 3–4. Pulses with similar current densities are gathered together (Figs. 12a, 12b for $|i_{\text{app}}| = 1.87$ A m$^{-2}$ and Figs. 12c, 12d for $|i_{\text{app}}| = 4.97$ A m$^{-2}$). Positive-current (Figs. 12a, 12c) and

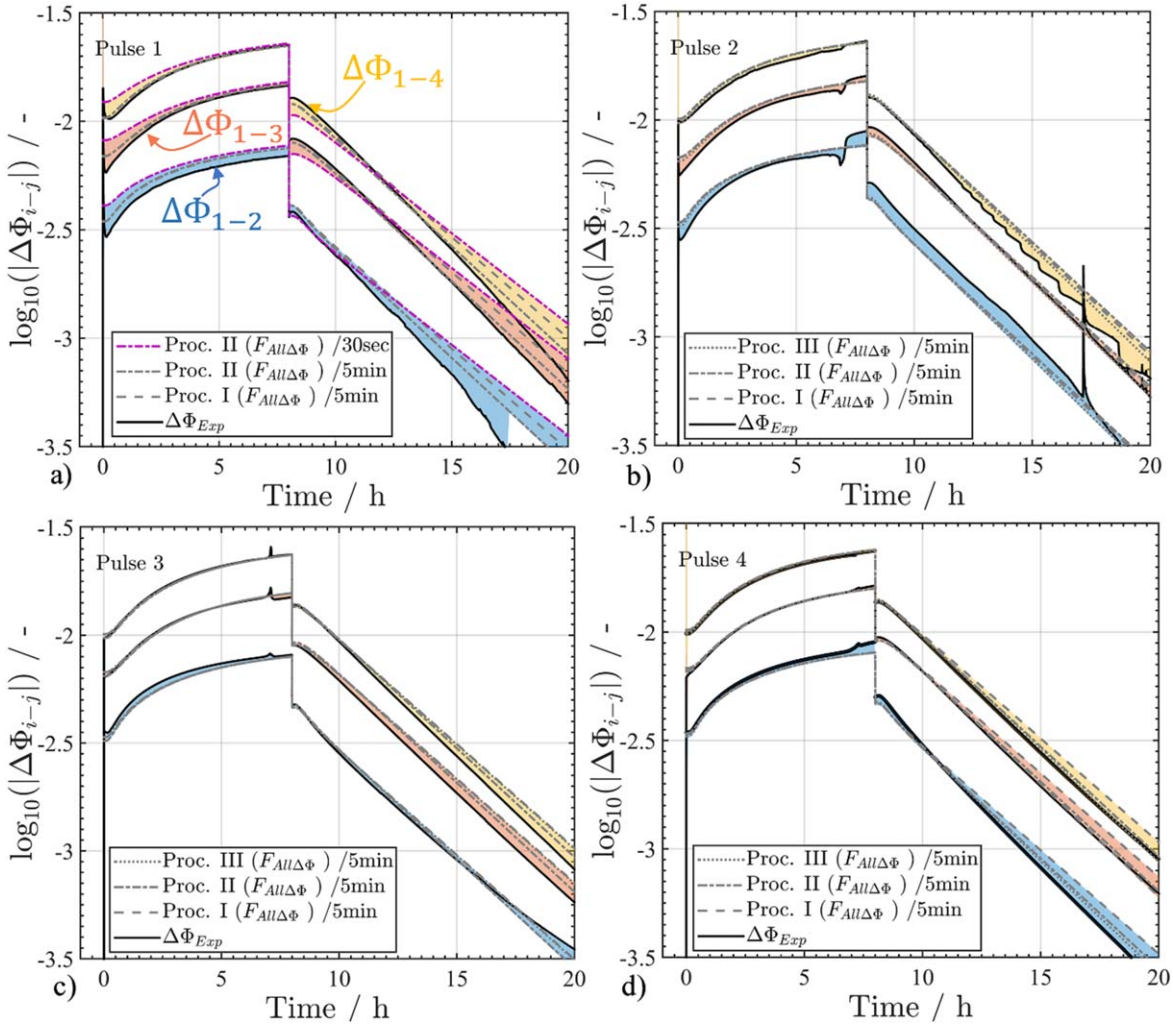


**Figure 9.** Comparison of nonlinear least-square regression results from three different parameter-estimation protocols (Table I) applied to the first four pulses (a)–(d). Experimental signals (solid black lines) are fitted using different protocols listed in Table I. The legend also indicates whether the first 30 seconds (purple lines) or 5 min (grey lines) of the cost functions $F_{All\Delta\Phi}$ are discarded for the evaluation of the goodness of fit. Procedure III is not represented on panel a) because it requires fixing $\kappa_{eff}$ which is underestimated due to the large voltage surge at the beginning of the pulse and leads to flawed results.

**Table I. Parameter values obtained with different curve-fitting protocols, averaged over nine successive pulses (pulses 2 to 10). First column indicates parameters that are numerically regressed. Nonmentioned parameters are computed using the aforementioned state-of-the art analytic methods. The intervals indicated between brackets refer to 95%-confidence intervals computed with the bootstrap method.**

| Optimized parameters | $D_{avg}$ ($m^2\ s^{-1}$) | $t^0_{+avg}$ | $N_{M\ avg}$ |
|---|---|---|---|
| I. $D$, $t^0_+$, $\kappa_{eff}$ | $2.57 \times 10^{-10}$ | 0.205 | 1.14 |
| | [± 3.06%] | [±9.68%] | [±1.63%] |
| II. $t^0_+$, $\kappa_{eff}$ | $2.65 \times 10^{-10}$ | 0.167 | 1.11 |
| | [±3.13%] | [±16.34%] | [±2.45%] |
| III. $t^0_+$ | $2.8 \times 10^{-10}$ | 0.204 | 1.15 |
| | [±2.63%] | [±25.9%] | [±4.11%] |
| IV. $D$, $t^0_+$ | $2.48 \times 10^{-10}$ | 0.24 | 1.18 |
| | [±5.09%] | [±27.1%] | [±5.00%] |

negative-current (Figs. 12b, 12d) pulses are superimposed on one another in separate panels. The figure shows signals of good quality, with reasonable reproducibility, despite the visible glitches during cycling. A careful comparison between Figs. 11c and 12 highlights that higher values of $N_M$ are indeed often associated with fitting procedures III and IV, and that signals of the corresponding pulses display strong onset voltage surges (for instance Pulses 7 and 9, Fig. 12).

In addition to average estimates, the confidence intervals are evaluated for each transport property (based on the dataset presented in Fig. 11), supplying information on the degree of reliability of the multi-electrode-cell method. Such confidence intervals may be evaluated using Student's $t$ distribution. However, this method requires that the data is sampled from a normally distributed population. The sets of 36 values for each fitted parameter represented in Fig. 11 display no evidence for such a requirement to be fulfilled (obvious distribution skewness, sample dependence on the determination procedure, possible bimodal distribution of $t^0_+$ and $N_M$…). This lack of normality is further illustrated in Fig. 13. The figure represents the initial dataset (Figs. 13a–13c), using 3 visualization tools: (i) the histogram is a direct observation of the distribution of values; (ii) the $Q$-$Q$ plot helps to assess whether the assumption of normal distribution of the data (blue dots) is reasonable (linear behavior according to the red line on the plot); (iii) the box plot allows a clear visualization of the distribution skewness (distribution of the values and straightforward comparison between the sample mean, represented by the blue horizontal line, and the median with the quartile $q_2$). It shows, in the initial sample, that

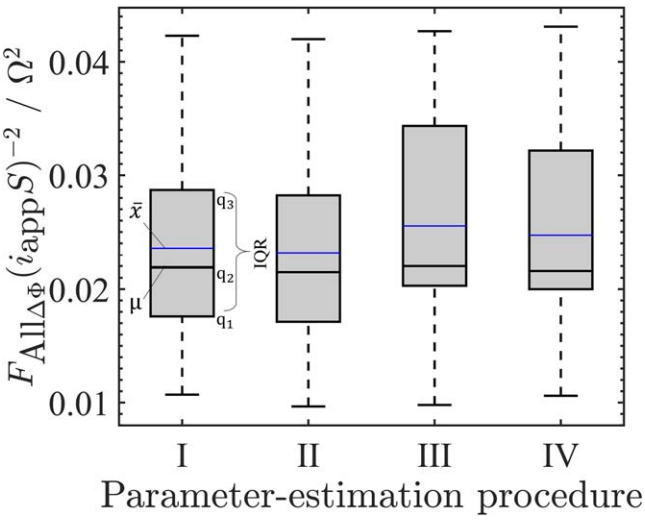


**Figure 10.** Boxplot diagrams illustrating the variations of the goodness of fit resulting from the minimization of $F_{\mathrm{All}\Delta\Phi}$, normalized by the square of the applied current $(i_{\mathrm{app}}S)^2$, among the four optimization procedures. The plot illustrates the distribution of the computed values of this quantity as a function of the optimization procedure in the following way: 25 % of the values are located under the line $q_1$, 50 % under the median value $\mu$ ($q_2$ horizontal line), and 75 % under $q_3$. Bottom and top whiskers contain values until 1.5 × IQR, where IQR stands for the inter-quartile range $q_3 - q_1$. The blue horizontal line represents the mean value.

although the distribution of parameter $D$ only seems to moderately depart from a normal distribution (Fig. 13a), the gap is more important for the distributions of $t_+^0$ (Fig. 13b) and $N_{\mathrm{M}}$ (Fig. 13c). Shapiro-Wilk's normality test provides another confirmation to these observations, as it validates the hypothesis of a probable normal distribution for the diffusion-coefficient values ($p \approx 0.15$) but rejects it for the values of $t_+^0$ ($p \approx 0.002$) and $N_{\mathrm{M}}$ ($p \approx 0.001$). Here, $p$-value $p$ denotes the probability of wrongly rejecting the normality hypothesis. The reliability of the computed 95% confidence intervals is then further assessed by comparing Student's $t$-distribution-based intervals with bootstrap-derived ones, which do not rely on the normality condition for the sample population.

500 bootstrap samples are thus generated by sampling with replacement from the original 36-element samples, for each fitted parameter (Figs. 13d–13f). The associated 95%-confidence intervals are constructed from the bootstrap sampling distribution (i.e. distribution of means of every bootstrap samples). Results of the computations are gathered in Table II.

Table II shows that both $t$-distribution and bootstrap-derived confidence intervals yield rather similar results. Considering the bootstrap confidence intervals, $D$ is determined with a total of 4.58% error centered around an average value of $2.62 \times 10^{-10}$ m$^2$ s$^{-1}$. $N_{\mathrm{M}}$ is centered around a value of $N_{\mathrm{M}} = 1.15$ within 3.48% of uncertainty. On the other hand, $t_+^0 = 0.204$, is determined within a 24.5% total error.

The high uncertainty in the value of $t_+^0$ may be partly explained by the method itself. A source of error is the already mentioned dispersion of values of the diffusion coefficient and McMullin Number, depending on the fitting procedure employed. Additionally, it is noteworthy that the anion transference number $t_-^0$ is the fitted parameter. The cationic transference number, which is much lower than the anionic one for the electrolyte studied here, is derived from the fitted $t_-^0$ (i.e., $t_+^0 = 1 - t_-^0$). A reasonable relative error in the determination of $t_-^0$ propagates a large relative error in the $t_+^0$. In this case, according to Table II, $t_-^0 = 0.796$ with a lower boundary of $t_{-\,\mathrm{lo}}^0 = 0.770$ and an upper boundary $t_{-\,\mathrm{up}}^0 = 0.820$. Error in $t_-^0$ thus drops back to ±3.14 % around $t_-^0$ (i.e., a total width of 6.28% for the error interval). With regular electrolytes used in actual commercial cells, $t_+^0$ is larger, hence we anticipate the confidence interval on $t_+^0$ would be much narrower than what is obtained here for 1 M $LiPF_6$ in EC/DEC 1:1 in wt.

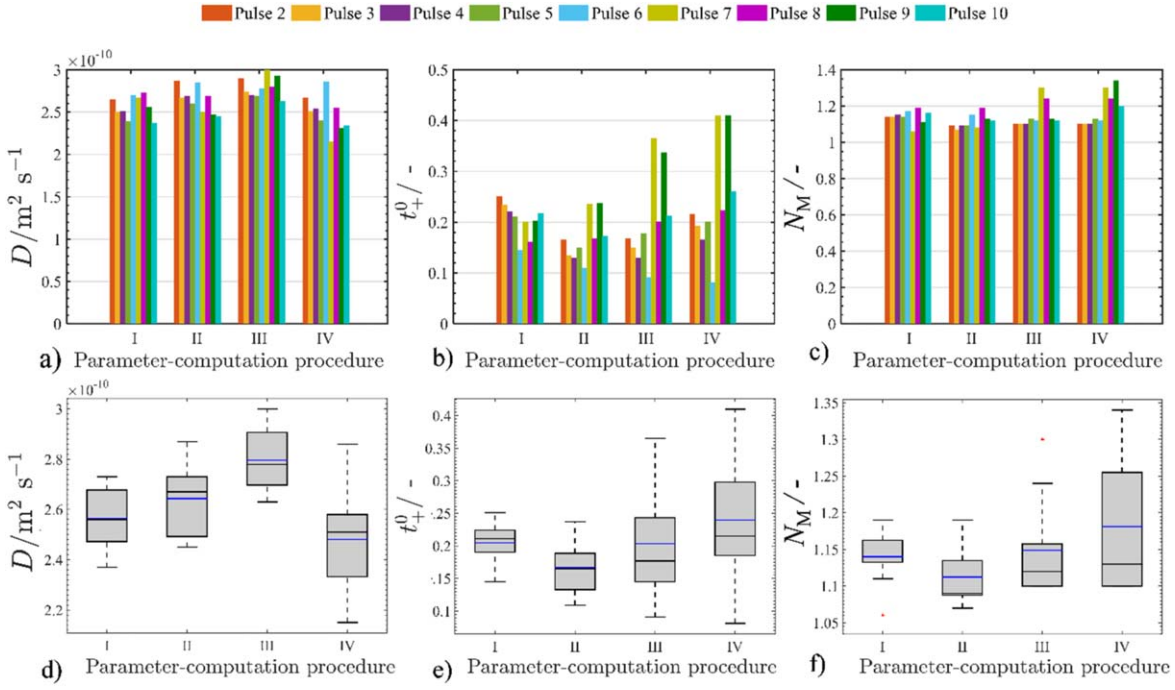


**Figure 11.** Detailed parameter estimation results for all nine pulses (Pulses 2 to 10), using the four fitting procedures (labelled I to IV in Table I). Marker and bar colors represent the pulse number, as indicated on the color code on top of the figure. (a) Diffusion coefficient $D$, (b) transference number $t_+^0$ and (c) McMullin number $N_{\mathrm{M}}$ are plotted vs both pulse number and fitting procedures. Boxplots (d)–(f) give a good visual insight about the distribution of the values of each parameter in the sample with respect to each determination procedure.

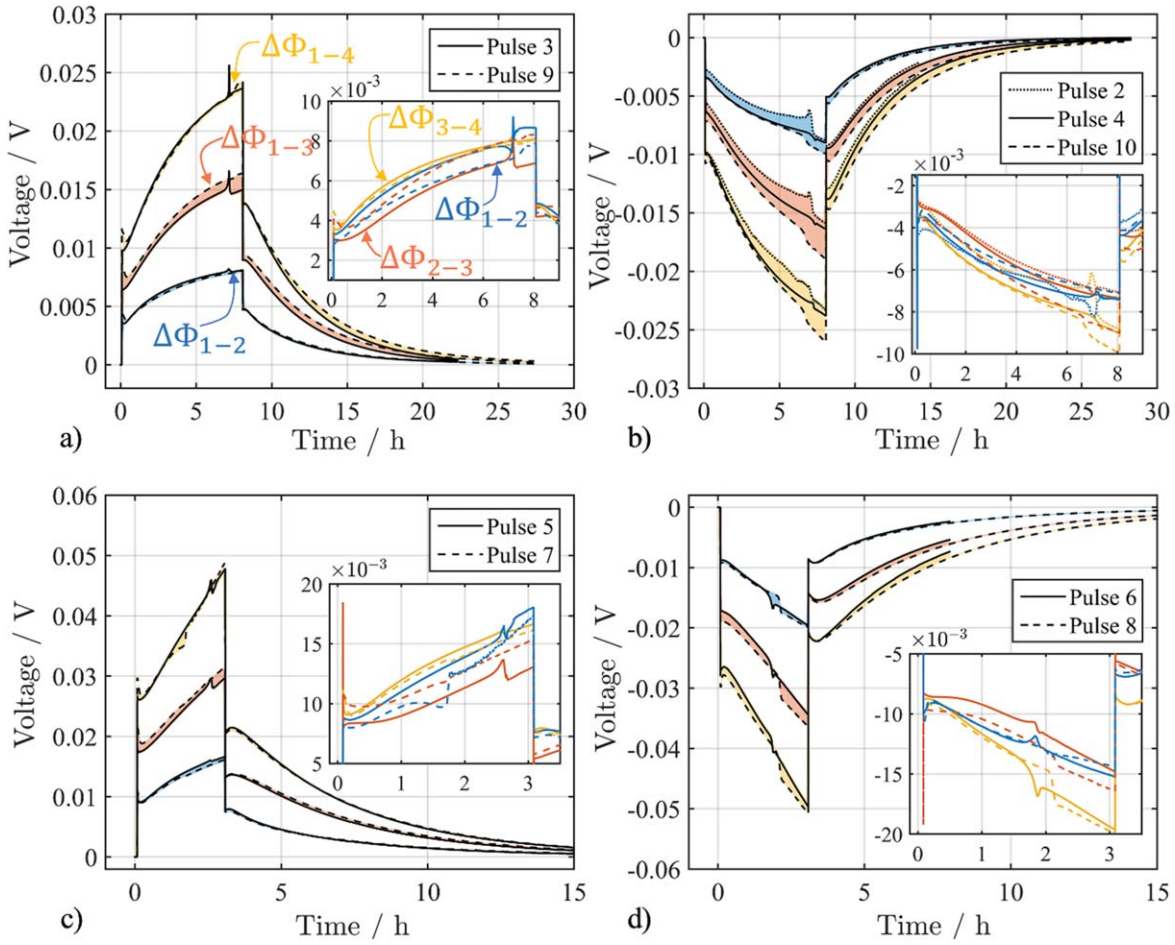


**Figure 12.** Raw $\Delta\Phi_{1-2}$, $\Delta\Phi_{1-3}$ and $\Delta\Phi_{1-4}$ data, for current densities (a) $i_{app} = 1.87$ A m$^{-2}$, (b) $i_{app} = -1.87$ A m$^{-2}$, (c) $i_{app} = 4.97$ A m$^{-2}$ and (d) $i_{app} = -4.97$ A m$^{-2}$. The corresponding $\Delta\Phi_{1-2}$, $\Delta\Phi_{2-3}$ and $\Delta\Phi_{3-4}$ signals are plotted in the inset of each panel.

At a first glance, the values determined for the different transport parameters look widely dispersed (especially for the $t_+^0$). However, it is important to look in detail at Fig. 14, which gathers parameter values from several literature sources for $D$ (Fig. 14a) and $t_+^0$ (Fig. 14b). Indeed, when the data presented in Fig. 13 and Table II is considered in the context of the state of the art, the error bars associated with the parameters are reasonable compared to the spread of values found in the literature (Fig. 14) for a similar liquid electrolyte (1M $LiPF_6$ in EC/DEC 1:1 wt.). Feng et al.'s[16] NMR-based parameter estimates seem to be higher than values estimated electrochemically, for $t_+^0$, with a value lying around $t_+^0 = 0.26$. Klett et al.,[6] who used NMR-MRI techniques coupled with numerical optimization, came up with a value of $t_+^0 = 0.20$. Although this value is very close to our measurement, the solvent used in their work is mixed with 15% in weight of poly(methyl methacrylate) (PMMA). The addition of PMMA aims at increasing viscosity to avoid convection in the electrolyte bulk. Ion transport may thus be influenced by this composition change and a different $t_+^0$ is expected without PMMA. Zugmann et al.[27] reported high values of $t_+^0$ for two different concentrations using electrochemical methods. Their value for a 1M electrolyte is located somewhere between $t_+^0 = 0.24$ and $t_+^0 = 0.34$. However, the small number of available data points and their apparent dispersion do not allow for accurate interpolation to the real value of the transference number at 1 mol L$^{-1}$. Farkhondeh et al.[35] found $t_+^0 = 0.267$, with a slightly different solvent (EC/DEC 1:1 in vol.). Lundgren et al.[28] reported a value of $t_+^0 = 0.162$, which may be directly compared with our work because it uses the exact same electrolyte formulation and the transport properties of the electrolyte are assessed using restricted-diffusion and inverse-modeling approaches. Diffusion coefficient estimates are also in good agreement with literature. Lundgren et al.[28] reported that $D = 2.53 \times 10^{-10}$ m$^2$ s$^{-1}$. Feng's value for $D$ (assessed using NMR techniques) is again slightly higher: $D = 3.26 \times 10^{-10}$ m$^2$ s$^{-1}$.[16] Farkhondeh reports $D = 2.45 \times 10^{-10}$ m$^2$ s$^{-1}$ for 1:1 vol. EC/DEC.[35]

## Conclusions

Transport properties of a 1M $LiPF_6$ in EC/DEC (1:1 in weight) are investigated in this work, using a multi-electrode cell. The device, based on that reported by Farkhondeh et al. in 2016,[34,35] consists in a Li-symmetric cell, comprising four Li reference electrodes evenly spaced along the cell thickness. The electrolyte is characterized by applying ten galvanostatic pulses (of current densities $|i_{app}| = 1.87$ A m$^{-2}$ and $|i_{app}| = 4.97$ A m$^{-2}$) of alternating signs to the cell. During a pulse (closed circuit and open-circuit relaxation steps), the voltage response of the electrolyte is measured between the available reference-electrode couples. The use of multiple reference electrodes ($N = 4$ in this study), in addition to the two working electrodes, enables a gain in information for the evaluation of the transport properties. Indeed, $N - 1$ independent voltage signals $\Delta\Phi_{m-n}$ can be measured between pairs of reference electrodes (with $m$ and $n$ being the reference electrode numbers, $m \neq n$). Voltage data are processed using four curve-fitting procedures, relying on a combination of analytic methods from the literature and/or numerical optimization.[8,25,28] On the one hand,

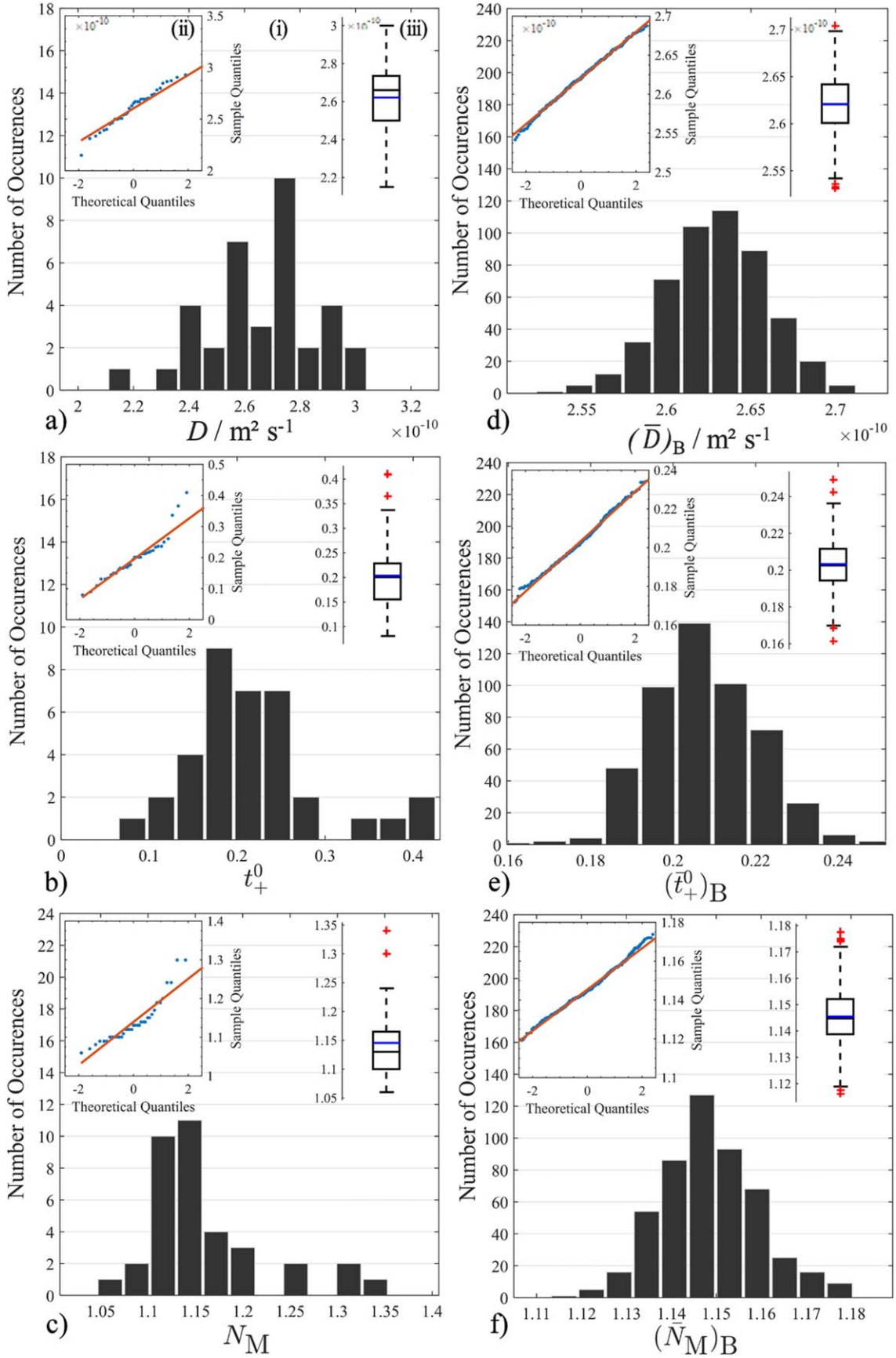


**Figure 13.** (a)–(c) Distribution of the parameters $D$, $t_+^0$ and $N_M$ estimated from nonlinear regression using the measured signals (initial 36-element samples). (d)–(f) Sampling distribution (distribution of the mean of each sample) of the set of 500 bootstrap samples generated using the initially measured sample of size 36. Each frame contains information gathered in three different plots: (i) a histogram, (ii) a *Q-Q* plot and (iii) a box plot.

**Table II. Average values of $D$, $t_+^0$, $t_-^0$ and $N_M$ obtained from galvanostatic pulses number 2 to 10 using four different fitting procedures, gathering 36 estimated values for each parameter. Corresponding 95% bilateral confidence intervals and error percentages are derived using two methods: Student's *t*distribution (computed using the raw dataset) and the bootstrap method. The lower and upper bounds of the confidence intervals, respectively $\theta_{lo}$ and $\theta_{up}$, for the generic parameter $\theta$ are reported in absolute values while the percentage of error is reported as a variation around the estimated average.**

| | Processing Method | $D$ ($m^2s^{-1}$) × $10^{-10}$ | | $t_+^0$ | | $t_-^0$ | | $N_M$ | |
|---|---|---|---|---|---|---|---|---|---|
| Mean | Base sample | 2.62 | | 0.204 | | 0.796 | | 1.15 | |
| | Bootstrap | 2.62 | | 0.204 | | 0.796 | | 1.15 | |
| Confidence Interval (CI) [$\theta_{lo}$\|$\theta_{up}$] | Student | 2.56 | 2.69 | 0.178 | 0.23 | 0.770 | 0.822 | 1.12 | 1.17 |
| | Std. Bootstrap | 2.56 | 2.68 | 0.180 | 0.23 | 0.770 | 0.820 | 1.13 | 1.17 |
| Percentage of error (+/-) | Base sample | 2.34 | | 13.1 | | 3.27 | | 2.23 | |
| | Std. Bootstrap | 2.29 | | 12.25 | | 3.14 | | 1.74 | |

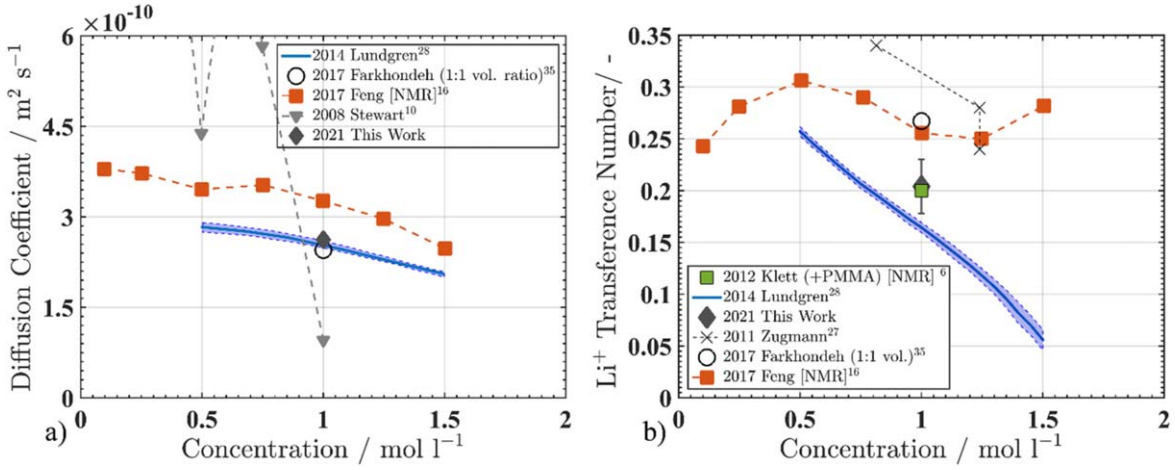


**Figure 14.** Parameters available in the literature for $LiPF_6$ in EC:DEC 1:1 (weight proportions, unless stated otherwise). (a) Diffusion coefficient; (b) transference number. Dashed connectors between markers are only for eye-guidance purpose.

the McMullin number $N_M$ and electrolyte diffusion coefficient $D$ can be derived separately using ohmic drops at short time (or high-frequency EIS) and voltage relaxation during OCV at long time, respectively. On the other hand, transference number $t_+^0$ is determined by nonlinear least-square regression on the three voltage signals $\Delta\Phi_{1-2}$, $\Delta\Phi_{2-3}$ and $\Delta\Phi_{3-4}$, simultaneously. The first parameter-estimation procedure (I) is based on the nonlinear regression of all parameters simultaneously. Procedure II consists in using numerical optimization for the estimation of both $N_M$ and $t_+^0$, while $D$ is obtained separately from the slope of $\ln(|\Delta\Phi_{m-n}|) - t$ curve during the OCV decrease. Regression of $t_+^0$ alone is performed in the third procedure (III), while $D$ and $N_M$ are derived using direct methods from the literature. Finally, in the fourth parameter estimation method, $N_M$ is obtained separately using ohmic drop at short time while regression is used to estimate $D$ and $t_+^0$. The results pertaining to these four determination procedures, individually, are shown in Table I, together with their associated bootstrap-computed 95% confidence intervals. The values display substantial variations and their relative errors are larger when using procedures involving separate calculation of $N_M$. The combined processing of the datasets from all four procedures allows for the computation of reliable averaged values and corresponding 95% confidence intervals: $D = 2.62 \times 10^{-10}$ [± 2.29 %] $m^2\ s^{-1}$, $t_+^0 = 0.204$ [±12.25 %] and $N_M = 1.15$ [± 1.78 %].

The dispersion observed in the parameter estimates is attributed to two main root causes: the method itself, and the experimental setup. While the relative error on fitting $t_-^0$ is reasonable, the relative error that results on $t_+^0$ is much larger due to its low intrinsic value for the electrolyte selected in this work. Parasitic effects due to Li-plating/stripping-related phenomena at the working electrodes (dendrite and passivation layer growth, dead Li trapped in Li moss etc.) are the other cause of estimate dispersion. The signals measured between the reference electrodes interact remotely with complex surface phenomena occurring at the Li working electrodes (distorting the current lines in the electrolyte). Such deviations from ideal signals lead to uncertainties in the values of the transport parameters, constituting the main limitation for this cell design. Due to their complex dynamics, it is not straightforward to account for these parasitic effects quantitatively. The use of electrodes with uniform surface dynamics would reduce the level of noise induced in the measured signals. We expect that either the use of porous electrodes or preconditioned Li electrodes instead of pristine Li working electrodes would be a good workaround to the problems observed at the working electrodes. Eventually, we expect that such an improvement would also enable the determination of concentration dependence of the transport parameters, using the reference electrodes to probe several delimited slices of electrolyte potential over the cell length. The multi-electrode cell may then, after solving these working electrode issues, become an efficient tool for the complete characterization of binary electrolytes.

## Acknowledgments

The authors would like to thank Tristan Lombard and François Rabuel (engineers at LRCS—UMR CNRS 7314) for the numerous insightful exchanges about experimental aspects of this project.

Jean-Paul Chehab (professor at LAMFA—UMR CNRS 7352) is also acknowledged for discussions about numerical optimization.

The project "Electrolyte Properties for Li-ion Batteries (EP4B)" is co-funded by the European Union through the "European Regional Development Fund (ERDF)" and the "Région Hauts-de-France." The authors are also grateful to the University of Picardy Jules Verne (UPJV) and to Mathieu Morcrette (director of LRCS) for granting extra financial supports, notably responding to the impact of COVID-19 on this research work.

## ORCID

C. Rabette https://orcid.org/0000-0003-4946-7106
M. Farkhondeh https://orcid.org/0000-0003-0960-8621
C. Delacourt https://orcid.org/0000-0001-5241-5441

## References

1. U.S. Department of Energy, *Energy Storage Grand Challenge : Energy Storage Market Report* (2020).
2. U.S. Department of Energy and US Environmental Protection Agency, (2021), Median Driving Range of All-Electric Vehicles Tops 250 Miles for Model Year 2020, https://energy.gov/eere/vehicles/articles/fotw-1167-january-4-2021-median-driving-range-all-electric-vehicles-tops-250.
3. Pod Point, (2020), How Long Does It Take to Charge an Electric Car?, https://pod-point.com/guides/driver/how-long-to-charge-an-electric-car.
4. S. Malifarge, B. Delobel, and C. Delacourt, *J. Electrochem. Soc.*, **164**, E3329 (2017).
5. J. S. Newman and K. E. Thomas-Alyea, *Electrochemical systems* (Wiley, Hoboken, New Jersey) 3rd ed. (2004).
6. M. Klett, M. Giesecke, A. Nyman, F. Hallberg, R. W. Lindström, G. Lindbergh, and I. Furó, *J. Am. Chem. Soc.*, **134**, 14654 (2012).
7. S. A. Krachkovskiy, J. D. Bazak, P. Werhun, B. J. Balcom, I. C. Halalay, and G. R. Goward, *J. Am. Chem. Soc.*, **138**, 7992 (2016).
8. A. Nyman, M. Behm, and G. Lindbergh, *Electrochim. Acta*, **53**, 6356 (2008).
9. S. Stewart and J. Newman, *J. Electrochem. Soc.*, **155**, A458 (2008).
10. S. G. Stewart and J. Newman, *J. Electrochem. Soc.*, **155**, F13 (2008).
11. L. O. Valøen and J. N. Reimers, *J. Electrochem. Soc.*, **152**, A882 (2005).
12. S. U. Kim and V. Srinivasan, *J. Electrochem. Soc.*, **163**, A2977 (2016).
13. G. Richardson, J. M. Foster, A. K. Sethurajan, S. A. Krachkovskiy, I. C. Halalay, G. R. Goward, and B. Protas, *J. Electrochem. Soc.*, **165**, H561 (2018).
14. H. S. Harned and D. M. French, *Ann. N. Y. Acad. Sci.*, **46**, 267 (1945).
15. P. G. Bruce and C. A. Vincent, *J. Electroanal. Chem.*, **225**, 1 (1987).
16. Z. Feng, K. Higa, K. S. Han, and V. Srinivasan, *J. Electrochem. Soc.*, **164**, A2434 (2017).
17. T. Hou and C. W. Monroe, *Electrochim. Acta*, **332**, 135085 (2020).
18. A. Sethurajan, S. Krachkovskiy, G. Goward, and B. Protas, *J. Comput. Chem.*, **40**, 740 (2019).
19. J. Landesfeind and H. A. Gasteiger, *J. Electrochem. Soc.*, **166**, A3079 (2019).
20. A. Ehrl, J. Landesfeind, W. A. Wall, and H. A. Gasteiger, *J. Electrochem. Soc.*, **164**, A2716 (2017).
21. A. Ehrl, J. Landesfeind, W. A. Wall, and H. A. Gasteiger, *J. Electrochem. Soc.*, **164**, A826 (2017).
22. N. P. Balsara and J. Newman, *J. Electrochem. Soc.*, **162**, A2720 (2015).
23. D. M. Pesko, S. Sawhney, J. Newman, and N. P. Balsara, *J. Electrochem. Soc.*, **165**, A3014 (2018).
24. P. Georén and G. Lindbergh, *Electrochim. Acta*, **49**, 3497 (2004).
25. Y. Ma, M. Doyle, T. F. Fuller, M. M. Doeff, L. C. D Jonghe, and J. Newman, *J. Electrochem. Soc.*, **142**, 1859 (1995).
26. D. A. Macinnes and L. G. Longsworth, *Chem. Rev.*, **11**, 171 (1932).
27. S. Zugmann, M. Fleischmann, M. Amereller, R. M. Gschwind, H. D. Wiemhöfer, and H. J. Gores, *Electrochim. Acta*, **56**, 3926 (2011).
28. H. Lundgren, M. Behm, and G. Lindbergh, *J. Electrochem. Soc.*, **162**, A413 (2014).
29. J. Newman and T. W. Chapman, *AIChE J.*, **19**, 343 (1973).
30. M. Doyle and J. Newman, *J. Electrochem. Soc.*, **142**, 3465 (1995).
31. D. Aurbach, *Solid State Ionics*, **148**, 405 (2002).
32. K. H. Chen, K. N. Wood, E. Kazyak, W. S. Lepage, A. L. Davis, A. J. Sanchez, and N. P. Dasgupta, *J. Mater. Chem. A*, **5**, 11671 (2017).
33. Q. Li, S. Tan, L. Li, Y. Lu, and Y. He, *Sci. Adv.*, **3**, 7 (2017).
34. M. Farkhondeh, M. Pritzker, M. Fowler, and C. Delacourt, *Electrochem. Commun.*, **67**, 11 (2016).
35. M. Farkhondeh, M. Pritzker, C. Delacourt, S. S. W. Liu, and M. Fowler, *J. Phys. Chem. C*, **121**, 4112 (2017).
36. M. Liu, S. J. Visco, and L. C. D. Jonghe, *Electrochim. Acta*, **38**, 1289 (1993).
37. J. Zhou, D. Danilov, and P. H. L. Notten, *Chem. - A Eur. J.*, **12**, 7125 (2006).
38. C. Delacourt, (2018), Dumbat, http://charles.delacourt.free.fr/dumbat.
39. T. F. Fuller, M. Doyle, and J. Newman, *J. Electrochem. Soc.*, **141**, 1 (1994).
40. C. Delacourt, P. L. Ridgway, V. Srinivasan, and V. Battaglia, *J. Electrochem. Soc.*, **161**, A1253 (2014).
41. M. Ender, J. Illig, and E. Ivers-Tiffée, *J. Electrochem. Soc.*, **164**, A71 (2017).
42. K. N. Wood, E. Kazyak, A. F. Chadwick, K.-H. Chen, K.-H. Zhang, K. Thornton, and N. P. Dasgupta, *ACS Cent. Sci.*, **2**, 11 (2016).
43. G. Bieker, M. Winter, and P. Bieker, *Phys. Chem. Chem. Phys.*, **17**, 8670 (2015).
44. D. Aurbach, B. Markovsky, G. Salitra, E. Markevich, Y. Talyossef, M. Koltypin, L. Nazar, B. Ellis, and D. Kovacheva, *J. Power Sources*, **165**, 491 (2007).